Role of Nanoparticle Size and Surface Chemistry on Ion Transport and Nanostructure of Perfluorosulfonic Acid Ionomer Nanocomposites

SCHOLARONE™
Manuscripts

Role of Nanoparticle Size and Surface Chemistry on Ion Transport and Nanostructure of Perfluorosulfonic Acid Ionomer Nanocomposites

Allison Domhoff[1],[‡], Xueting Wang[1], [‡], Mayura S. Silva[2], Stephen Creager[2], Tyler B. Martin[3], and Eric M. Davis[1],*

[‡]indicates equal contribution

[1]Department of Chemical and Biomolecular Engineering, Clemson University, Clemson, South Carolina 29634, United States

[2]Department of Chemistry, Clemson University, Clemson, South Carolina 29634, United States

[3]National Institute of Standards and Technology (NIST), Gaithersburg, Maryland 20899, United States

[†]indicates equal contribution

*To whom correspondence should be addressed: ericd@clemson.edu

ABSTRACT:

Herein, we present a systematic investigation of the impact of silica nanoparticle (SiNP) size and surface chemistry on the nanoparticle dispersion state and the resulting morphology and vanadium ion permeability of the composite ionomer membranes. Specifically, Nafion containing a mass fraction of 5% silica particles, ranging in nominal diameters from 10 nm to >1 μm and with both sulfonic acid- and amine-functionalized surfaces, were fabricated. Most notably, an 80% reduction in vanadium ion permeability was observed for ionomer membranes containing amine-functionalized SiNPs at a nominal diameter of 200 nm. Further, these membranes exhibited an almost 400% increase in proton selectivity when compared to pristine Nafion. Trends in vanadium ion permeability within a particular nominal diameter were seen to

be a function of the surface chemistry, where, for example, vanadyl ion permeability was observed to increase with increasing particle size for membranes containing unfunctionalized SiNPs, while it was seen to remain relatively constant for membranes containing amine-functionalized SiNPs. In general, the silica particles tended to exhibit a higher extent of aggregation as the size of the particles was increased. From small-angle neutron scattering experiments, an increase in the spacing of the hydrophobic domains was observed for all composite membranes, though particle size and surface chemistry were seen to have varying impacts on the spacing of the ionic domains of the ionomer.

1. Introduction

Perfluorosulfonic acid (PFSA) ionomer membranes are ubiquitous polymer electrolyte membranes (PEMs) for flow battery and fuel cell applications.[1–4] Specifically, vanadium redox flow batteries (VRFBs) benefit from PFSA ionomer PEMs due to their nanophase segregation, where, under hydration, ionic (hydrophilic) domains allow for high proton conductivity (oftentimes referred to as water-assisted ion transport),[5] while the hydrophobic backbone provides both chemical and mechanical stability, which is of particular importance under the highly oxidative conditions (approximately 3 mol L^{-1} sulfuric acid and similar concentrations of V(5+)) of the VRFB.[4,6–8] However, one standing issue with Nafion,[9] the canonical PFSA ionomer standard, as well as other similar PFSA ionomers, is their low ion selectivity, as facile transport of both protons and vanadium ions occurs through the hydrated ionic domains.[10–12]

To combat the observed low ion selectivity of traditional PFSA ionomers, the incorporation of nanoparticles, specifically silica nanoparticles (SiNPs), has been shown to increase the selectivity of the ionomer membranes.[10,11,13,14] There are two primary methods utilized to incorporate SiNPs into PFSA ionomers: (1) in-situ, sol-gel condensation and (2) solution casting ionomer dispersions containing discrete SiNPs. Sol-gel nanocomposite membrane fabrication modifies the well-known Stöber synthesis of SiNPs by simply incorporating the SiNP precursors, usually tetraethylorthosilicate (TEOS), into an extruded (i.e., pre-formed) PFSA ionomer.[15–17] The sulfonic acid pendant chains, in place of base in typical Stöber synthesis, facilitate the formation of SiNPs as the silicate precursor is hydrolyzed, and condensation occurs, allowing for the nucleation and growth of SiNPs within the pre-formed membrane.[16–20] Importantly, the SiNPs are restricted to form within the structure of the swollen membrane.[20] It is generally theorized that the SiNPs form within the ionic domains of the membrane (swollen in a mixture of

methanol and water), where the TEOS condensation reaction is catalyzed by the sulfonic acid groups in the presense of water.[17,20] While water will appreciably swell the ionic domains, methanol swells the hydrophobic domain as well.[21–23] Additionally, it has been observed that acid-catalyzed SiNP formation creates a gel-like structure rather than discrete particles.[24] Thus, the SiNP gel can hypothetically form anywhere within the PFSA structure. Alternatively, solution cast membranes are created by the incorporation of discrete pre-formed SiNPs into a PFSA ionomer dispersion, which is mixed before casting for solvent evaporation.[13,25,26] Solution casting removes the unknown and uncontrollable SiNP formation that occurs within the PFSA matrix and allows tunable dispersions to be produced.[6,27] Additionally, SiNP surface chemistry and size can be specifically controlled and varied before the incorporation into the nanocomposite dispersion. The SiNP surface characteristics (e.g., charge, chemistry of bridging chain, grafting density) are expected to play an important role in controlling the dispersion state, and in turn, the nanostructure and performance properties of the resulting ionomer nanocomposites.[27,28] Lastly, sol-gel solution cast membranes combine both techniques by incorporating SiNP precursors into PFSA ionomer dispersion before solvent is evaporated to form nanocomposite membranes.[29–32]

All nanocomposite fabrication methods have been utilized in literature in efforts to reduce either vanadium ion crossover (for VRFBs) or methanol crossover (for direct methanol fuel cells), but the dispersion of the SiNPs and the resultant nanocomposite morphology are rarely investigated to relate specifically to the increased ion selectivity.[6,27,28] It is generally assumed, as previously mentioned, that SiNPs reside within the ionic domain, and that their presence hinders the passage of bulky hydrated vanadium ions while still allowing protons to conduct through the membrane.[11,33,34] However, recent investigations have demonstrated that SiNPs formed by sol-

gel or incorporated by solution casting are much too large to fit entirely within the ionic domain, which is again only 3 nm to 5 nm in diameter when hydrated.[6,35] Additionally, most literature sources fail to even consider the size of the SiNPs formed by sol-gel or utilized in solution casting. SiNPs are inexpensive and readily available for purchase through numerous suppliers, but even SiNPs bought with nominal sizes on the order of the ionic domain that have been dried can create massive aggregates that negates the nominal size altogether. It is well-known that drying causes irreversible aggregation of SiNPs,[36,37] so it is crucial to investigate the dispersion of SiNPs after incorporation in the nanocomposite membrane whether by sol-gel or solution casting.

If the SiNPs are not blocking the ionic domains to reduce vanadium ion crossover, it is curious how the introduction of such inorganic fillers could affect the selectivity of the membranes. Di Noto and coworkers have proposed a peristaltic-like motion of the ionic domain and hydrophobic backbone to facilitate ion transport through Nafion-SiO$_2$ membranes for proton exchange membrane fuel cells.[38,39] Other recent work has suggested that SiNPs reside at the interface of the ionic and hydrophobic domains,[40,41] which could slow down the peristaltic motions of the membrane to cause reduction in vanadium ion permeability. However, to the best of the authors' knowledge, there has yet to be a systematic investigation into the incorporation of a variety of controlled sizes and NP surface chemistries into the ionomer matrix. Our present work aims to bridge this knowledge gap.

In this work, PFSA–SiO$_2$ nanocomposites were fabricated via solution casting dispersions of Nafion containing a mass fraction of 5% SiNPs with various surface functionalizations and nominal diameters. This silica mass fraction is similar to those used by others in the literature and is consistent was previous research from our group. The nominal diameter of the SiNPs

ranged from approximately 10 nm (i.e., NPs sized on the order of the ionic domains) to >1 μm. The surface functionalities of SiNPs were chosen such that they would electrostatically interact with the sulfonic acid ionic groups, where the surface chemistry was varied from unfunctionalized (i.e., hydroxyl-coated), sulfonic-acid functionality, and amine functionality. We investigate the ion transport properties of the nanocomposites by measuring the vanadium (IV) ion (vanadyl ion; VO^{2+}) permeability, proton conductivity, and ion-exchange capacity (IEC) of each membrane. Additionally, both transmission electron microscopy (TEM) and optical microscopy were utilized to characterize SiNP dispersion state within the nanocomposite membranes. Finally, small-angle neutron scattering (SANS) was employed to characterize the morphology of the hydrated PFSA ionomer nanocomposites.

2. Materials and Methods

2.1. Materials

Ethanol (pure, 200 proof, anhydrous), sulfuric acid (95% to 98%, ACS Reagent), vanadium (IV) oxide sulfate hydrate (97%), magnesium sulfate (anhydrous), and (3-mercaptopropyl)trimethoxysilane (95%) (MPTMS) were purchased from Sigma Aldrich. Nafion stock dispersion (Nafion D2021) was purchased from Ion Power. Hydrogen peroxide (30%) was purchased from VWR Analytical. 3-aminopropyltrimethoxysilane (97+%) (APTMS) was purchased from TCI Chemicals. Unfunctionalized silica nanoparticles (SiNPs) denoted as UF–10 (colloidal silica in methanol; MT-ST grade; D_P = (10 to 15) nm, where D_P is the particle diameter), unfunctionalized SiNPs denoted as UF–100 (colloidal silica in isopropyl alcohol; IPA–ST–L; D_P = (40 to 50) nm), and unfunctionalized SiNPs denoted as UF–200 (colloidal silica in isopropyl alcohol; IPA–ST–ZL; D_P = (70 to 100) nm) were obtained from Nissan

Nanomaterials. Unfunctionalized SiNPs denoted as UF–dried (SiO_2, 99.5%, 20 nm, nonporous) and amine-functionalized SiNP denoted as AA-dried (SiO_2, 99.8%, (10 to 20) nm, surface modified with amino group) were purchased from SkySpring Nanomaterials, Inc. Reverse osmosis (RO) water (resistivity of approximately 18 MΩ cm) was used for all experiments. Note, all particle sizes, and size ranges, noted in parentheses are those specified by the product manufacturers, while the numbers included in the membrane notation (shown in Table 1) are nominal (i.e., approximate) particle sizes as visually determined by electron and optical microscopy.

2.2. Membrane Preparation

The SiNPs were functionalized as previously described.[27,28] In general, the appropriate reagents were added to a suspension of unfunctionalized SiNPs, allowed to react, then washed and separated by centrifugation. All membranes were cast from the as-received Nafion dispersion. To incorporate the SiNPs, a mass fraction of 5% of either the functionalized or unfunctionalized SiNPs (mass of SiNPs/total mass of solids $\times$ 100%) were suspended in the Nafion dispersion by sonication for at least 30 min prior to casting. Pristine Nafion suspension (i.e., no SiNPs) was also sonicated for at least 30 min prior to casting. The Nafion suspensions were then cast onto a polished quartz substrate, covered by funnel with Kim-wipe flue, and allowed to evaporate overnight on the benchtop. The dried hybrid films were then annealed at 140 °C for 2 h under dynamic vacuum, after which the oven was shut off and dynamic vacuum was pulled for an additional 30 min. Afterwards, the valve to the vacuum pump was closed and the films were left to cool down to room temperature under static vacuum. Prior to beginning

measurements, the films were hydrated in RO water overnight. Hydrated film thicknesses were on the order of approximately 50 μm.

2.3. Vanadium ion permeability characterization

Vanadium ion crossover was measured as previously described.[27,28] Briefly, a tailor-made diffusion cell (Permegear Franz cell; Bethlehem, PA) was used. Shown below, the receiving cell (volume of 15 mL) was filled with a 1.5 mol L^{-1} $MgSO_4$ in 3 mol L^{-1} H_2SO_4 solution, and the donating cell (volume of 1 mL) was filled with a 1.5 mol L^{-1} $VOSO_4$ in 3 mol L^{-1} H_2SO_4 solution, where the membrane being tested (in this case, a perfluorosulfonic acid (PFSA) ionomer nanocomposite) was sandwiched between the two cells.
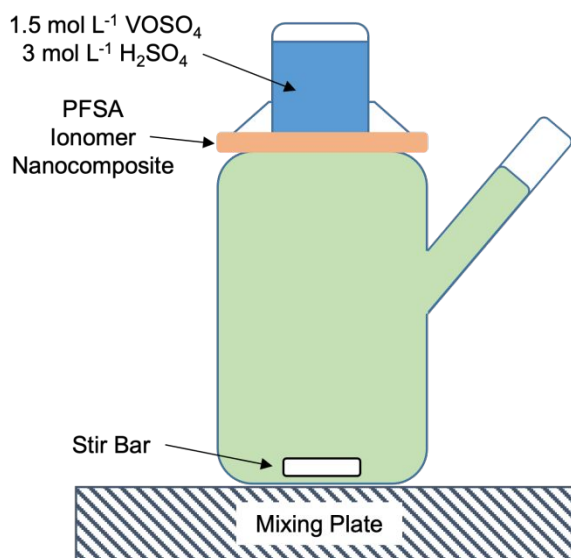
Figure 1. Schematic of the permeation cell used to measure vanadyl ion permeability through the perfluorosulfonic acid (PFSA) ionomer nanocomposites.

Aliquots were taken via the side arm of the receiving cell at regular time intervals, and the concentration of vanadium (IV) ions (vanadyl ion; VO^{2+}) was measured using a ultraviolet-visible (UV-vis) spectrometer (VWR UV-3100PC), which scanned from wavelengths of 1100 nm to 400 nm. The peak associated with the presence of VO^{2+} can clearly be observed around a wavelength of 760 nm. Immediately following UV-vis characterization, the aliquots were placed back into the receiving cell. From these data, the permeability of vanadium ions can be calculated using the following equation

$$V_R \frac{dC_R(t)}{dt} = A\frac{P}{L}C_D \quad ,$$ (1)

where C_D and $C_R(t)$ are the vanadium ion concentration in the donating and receiving cells (in mol L⁻¹), respectively, A and L are the area (in cm²) and thickness of the membrane (in cm), respectively, P is the permeability of VO^{2+} ions (in cm²-s⁻¹), and V_R is the volume of the receiving cell (L). This expression assumes the following: (1) the permeation in the membrane has reached pseudo-steady state, (2) vanadium ion permeability is independent of ion concentration, (3) $C_D \gg C_R(t)$, and (4) the reduction in C_D over the length of the experiment is negligible.[44]

2.4. Ion exchange capacity (IEC)

IEC experiments were performed according to literature.[27,45] Briefly, the membrane was dried under vacuum at 80 °C for 24 h, massed, and immersed in 1 mol L⁻¹ NaCl for 24 h. Next, the membrane was removed from the NaCl solution, and the remaining solution was titrated with 0.01 mol L⁻¹ NaOH with phenolphthalein (1% in a mixture of 1:1 water:ethanol by volume). The IEC for each membrane was calculated as follows

$$\text{IEC} = \frac{V_{\text{NaOH}}C_{\text{NaOH}}}{m_{\text{dry}}} \quad , \qquad \qquad (2)$$

where V_{NaOH} is the volume of titrated NaOH solution (in L), C_{NaOH} is the concentration of the NaOH solution, and m_{dry} is the dry mass of the membrane.

2.5. Equilibrium Water Uptake

After fabrication, each membrane was immersed in RO water and allowed to equilibrate for at least 24 h. Once the membranes were equilibrated, they were removed from the RO water, patted dry with a Kim Wipe, and the mass of the wet membrane, m_{wet}, was taken. To obtain the dry mass, the membranes were dried at 90 °C for 24 h. The following equation was used to calculate the equilibrium water uptake

$$\text{Equilibrium Water Uptake (\%)} = \frac{m_{\text{wet}} - m_{\text{dry}}}{m_{\text{dry}}} \times 100 \quad . \qquad \qquad (3)$$

2.6. Proton Conductivity and Selectivity

Through-plane proton conductivity was measured using a polymer electrolyte membrane (PEM) electrochemical hydrogen pump (H-pump) cell. Prior to running conductivity experiments, the membranes were pre-treated in 0.5 mol L^{-1} H$_2$SO$_4$ at 70 °C for 1 h, then stored in DI water until they were mounted in the H-pump cell. Electrodes (2 mg cm^{-2} Pt/C (Pt on Carbon cloth, Fuel Cell Store)) were attached to graphite rods (current collectors), and the graphite rods were pressed onto the membrane surface to define an active electrode area. Each side of the cell was bathed with humidified hydrogen gas, and symmetrical electrochemical H-pump experiments were carried out at 100% relative humidity and room temperature. These measurements provided

linear current–voltage curves reflecting proton transmission rates through the membranes. A WaveDriver 20 potentiostat/galvanostat system (Pine Research Instrumentation) was utilized for data collection, and AfterMath data organizer software (Pine Research) was utilized to analyze the data. Membrane resistance was calculated from the inverse slope of linear current−voltage curves, following correction for series resistance contributions from all other factors besides the membrane ohmic resistance. Membrane ionic conductivity κ was obtained from membrane resistance by accounting for geometric factors (area and thickness) using the following equation: $\kappa = d/RA$, where $\kappa, d,$ and R are the conductivity, thickness, and resistance of the membrane, respecitively, and A is the geometric active area for electrodes in the electrochemical H-pump cell. Additional information regarding the apparatus, along with an illustrative schematic, may be found elsewhere.[46]

From the proton conductivity and vanadium ion permeability, the proton selectivity S for each membrane can be calculated as follows

$$S = \frac{\kappa}{P} \qquad . \qquad (4)$$

2.7. Transmission electron microscopy (TEM) imaging

TEM samples were prepared according to literature. Briefly, dispersions of Nafion and SiNPs were diluted to a mass fraction of approximately (0.05% to 0.1%) Nafion in the same solvent as the solution. The solutions were drop cast onto 300 mesh copper grids with lacey carbon support (Electron Microscopy Services, Hatfield, PA), allowed to dry at room temperature, and annealed like previously described. The samples were then imaged by a Hitachi 9500 high-resolution

TEM operated at 300 kV, emission current of 8.0 μA, and filament of 29.1 V with an exposure time of 2.0 s.

2.8. Optical Microscopy Imaging

Composite films with dried particles were imaged by optical microscopy on an Olympus BX60 microscope with a 20x objective and using Image-Pro Plus software for image processing. Films were dried in the hood before imaging and adhered to a glass slide with double-sided tape. A cross-polarized lens was utilized for imaging.

2.9. Small-angle neutron scattering (SANS)

SANS experiments were performed on the NG-B 10 m SANS instrument (all samples except the membranes with "Dried" particles) and the NG-7 30 m SANS instrument (all samples prepared with the "Dried" particles) at the National Institute of Standards and Technology Center for Neutron Research (NCNR). Nanocomposite films were cast and annealed as described in the previous section. At least 24 h prior to SANS experiments, the membranes were hydrated in liquid H_2O. The hydrated films were then placed in a demountable cell, where the distance between quartz windows was either 1 mm or 2 mm. A circular aperture with diameter of 1.27 cm (or 0.5 in) was utilized for all samples. The incoming neutron wavelength and the sample-to-detector distance were varied to collect a range of Q values ($Q = 4\pi\sin\theta/\lambda$), where θ and λ are the scattering angle and wavelength of the neutrons, respectively. In this study, SANS data were collected over Q values ranging from 0.0035 Å^{-1} to 0.5 Å^{-1} for the 10 m SANS instrument and 0.0009 Å^{-1} to 0.5 Å^{-1} for the 30 m SANS instrument. The total collection time for each sample was approximately 3 h. The SANS data were reduced using the software package developed at the NCNR,[42] where the thickness of the cell was used for all reduction calculations. Furthermore,

both the high-Q (i.e., hydrophobic peak) and low-Q (i.e., hydrophilic or ionic peak) were fit to a

Gaussain model using SasView, which is available free of charge at https://www.sasview.org.

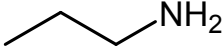## 2.10. Dynamic Light Scattering (DLS)

DLS was utilized to measure the hydrodynamic diameter of AA-Dried particle with a

ZetaSizer Nano ZS. Particles were suspended in RO water and sonicated for 30 min before
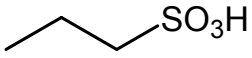
analysis.

3. Results and Discussions

3.1. Vanadium ion permeability, ion exchange capacity, and equilibrium water uptake

Table 1 summarizes the nomenclature for each of the PFSA ionomer nanocomposites

synthesized with respect to both the surface chemistry and the size of the SiNPs.

Table 1. Nomenclature for Nafion and Nafion nanocomposites containing a mass
fraction of 5% unfunctionalized and functionalized SiNPs with nominal diameters
ranging from 10 nm to >1 μm.

PFSA Membrane (-)	SiNP Surface Chemistry (-)	Nanoparticle Size (nm)	Nomenclature (-)
Nafion containing			
no SiNPs	N/A	N/A	Pristine–Naf
Unfunctionalized SiNPs (UF–SiNP)	—OH	10	Naf–UF–10
		100	Naf–UF–100
		200	Naf–UF–200
		>1000	Naf–UF–Dried
Alkyl-Amine SiNPs (AA–SiNP)	⁀NH$_2$	10	Naf–AA–10
		100	Naf–AA–100

		200	Naf–AA–200
		>1000	Naf–AA–Dried
Alkyl-Sulfonic Acid SiNPs (AS–SiNP)	$\diagup\!\!\diagdown\!\!\diagup\!\!\diagdown SO_3H$	10	Naf–AS–10
		100	Naf–AS–100
		200	Naf–AS–200
		>1000	Naf–AS–Dried

For example, the nomenclature for a PFSA ionomer containing a mass fraction of 5% unfunctionalized SiNPs, with an approximate diameter of 100 nm, is referred to as Naf–UF–100. Note, the SiNPs sizes listed in Table 1 are approximate sizes of the particles (determined via electron and optical microscopy imaging). Further, the term "Dried" is used to denote SiNPs that were received in a dry form, while all other SiNPs were purchased already suspended in solution and never dried out before being mixed with the PFSA ionomer prior to solution casting. The exact extent of aggregation of the Dried SiNPs is addressed later, as it is well-known that drying SiNPs results in significant and irreversible aggregation.[36,37]

Figure 2 shows the vanadyl ion (VO^{2+}) permeability of each ionomer nanocomposite as a function of both the size (numbers on the x-axis) and the surface chemistry (various colored bars) of the SiNPs, where solid gray, blue, and red bars represent membranes containing UF–
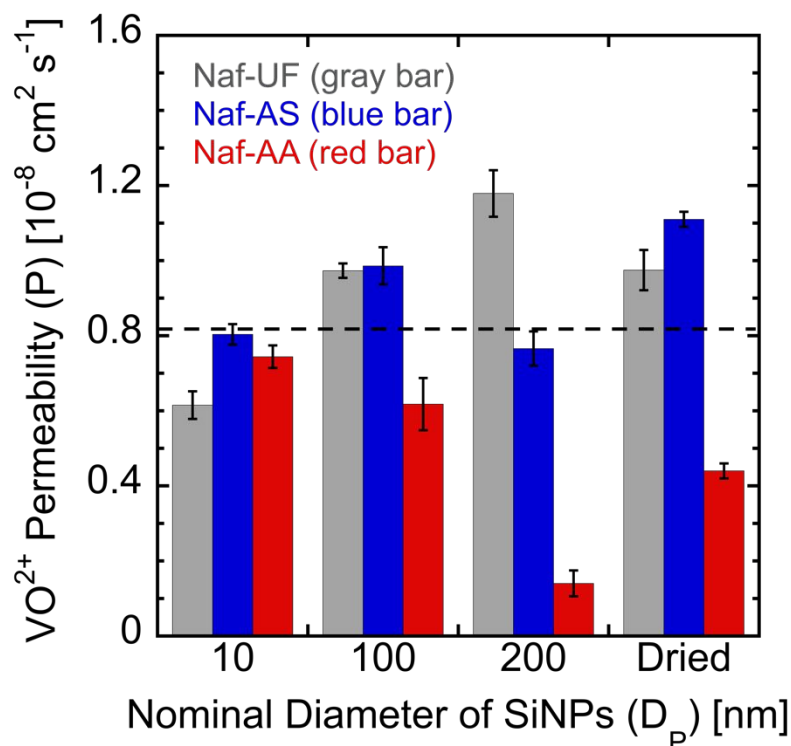
Figure 2. Vanadyl ion (VO^{2+}) permeability for PFSA ionomer nanocomposites containing a mass fraction of 5% SiNPs with varying nominal diameters and surface functionalities. Ionomer membranes containing UF-SiNP, AS-SiNP, and AA-SiNP are shown in solid gray, blue, and red bars, respectively. Error bars represent the standard deviation of the average VO^{2+} permeability, which was calculated from experiments on at least three separate membranes. The dashed black line represents the average VO^{2+} permeability for Pristine–Naf. Note, the data shown for membranes containing 10 nm SiNPs have been previously published.[27]

SiNP, AS–SiNP, and AA–SiNPs, respectively. As noted earlier, each of the nanocomposites contain a mass fraction of 5% SiNPs. For reference, a value of $(0.81 \pm 0.05) \times 10^{-8}$ cm^2 s^{-1} for the VO^{2+} permeability for pristine (no SiNPs), annealed Nafion membranes has previously been reported.[27] Focusing our attention in Figure 2 on ionomer membranes containing unfunctionalized SiNPs (i.e., containing UF–SiNP; solid gray (left) bars), we observe an initial,

statistically significant fractional increase of approximately 50% in vanadyl ion permeability

when the NP size is increased 10-fold. Note, the statistical significance in the difference between

various samples was determined from the p value obtained from a t-test on the data sets. As

shown in Figure 2, a difference in the calculated permeability between two samples can be

considered statistically significant if the ranges of each measured value (determined from the

average +/- the standard deviation) do not overlap. So, while the difference in VO^{2+}

permeabilities between Naf–UF–10 and Naf–UF–100 is statistically significant, the same is not

true when comparing Naf–UF–10 and Naf–AA–100, where, within the error on the calculated

average, the difference in permeabilities between these two samples is not statistically

significant. We observe a further increase in VO^{2+} permeability with increasing NP size, where a

fractional increase of over 100% is observed for Naf–UF–200, when compared to Naf–UF–10.

Note, Naf–UF–10 were the only membranes within this series of ionomer nanocomposites (i.e.,

those containing UF–SiNP) to exhibit a lower VO^{2+} permeability than that of annealed, solution-

cast Nafion containing no SiNPs (shown as the dashed black line in Figure 2).[6,27]

Next, focusing our attention on composite membranes containing alkyl-sulfonic acid-

functionalized SiNPs (i.e., containing AS–SiNP; solid blue (middle) bars), we observe that the

vanadyl ion permeabilities of all these composites were similar to or greater than the VO^{2+}

permeability of the Pristine–Naf membranes. Specifically, there were no statistically significant

differences among the permeabilities of Naf–AS–10, Naf–AS–200, and Pristine–Naf.

Additionally, as seen in Figure 2, there is no discernable trend in VO^{2+} permeability with NP

diameter for this series of membranes. Notably, the highest vanadium ion permeability

(approximately 50% larger than Pristine–Naf) was observed for Naf–UF–200 and Naf–AS–

Dried. In constrast, for composite membranes containing amine-functionalized SiNPs (i.e.,

containing AA–SiNP; solid red (right) bars), we observe NP size dependency in the VO^{2+} permeabilities, where an approximately 80% and 45% relative reduction in permeability (compared to Pristine–Naf) was observed for Naf–AA–200 and Naf–AA–Dried, respectively. In general, PFSA composite membranes containing AA–SiNP exhibited the lowest VO^{2+} permeabilities at each of the nominal NP sizes. The exception to this are composite membranes containing 10 nm SiNPs, where Naf–UF–10 showed a lower permeability than Naf–AA–10.

In addition to VO^{2+} permeability, the ion exchange capacity (IEC) and equilibrium water

uptake of each membrane were measured, and the results are presented in Figure 3. For

reference, the average IEC (1.03 ± 0.05 mmol g^{-1}) and equilibrium water uptake ($16.5 \pm 1.8\%$) of

Pristine–Naf are represented by the dashed black lines in Figures 3a and 3b, respectively.[47] The

IEC of an ionomer is an important parameter when discussing proton exchange membranes, as it

provides information on the amount of protons that are available for ion transport. This is closely

related to proton conductivity since ion hopping is one of the dominant mechanisms of proton

transport in ionomers. That is, a higher IEC indicates more protons available for the ion hopping

26

process, and thus (in theory) a higher proton conductivity. Water uptake is another factor that

might affect the proton conductivity, as the proton transport in these ionomers is a water-

28

facilitated process. The vehicular mechanism is the other mechanism of proton transport, where

29

freely moving water within the ion channels plays an essential role in transporting protons, and
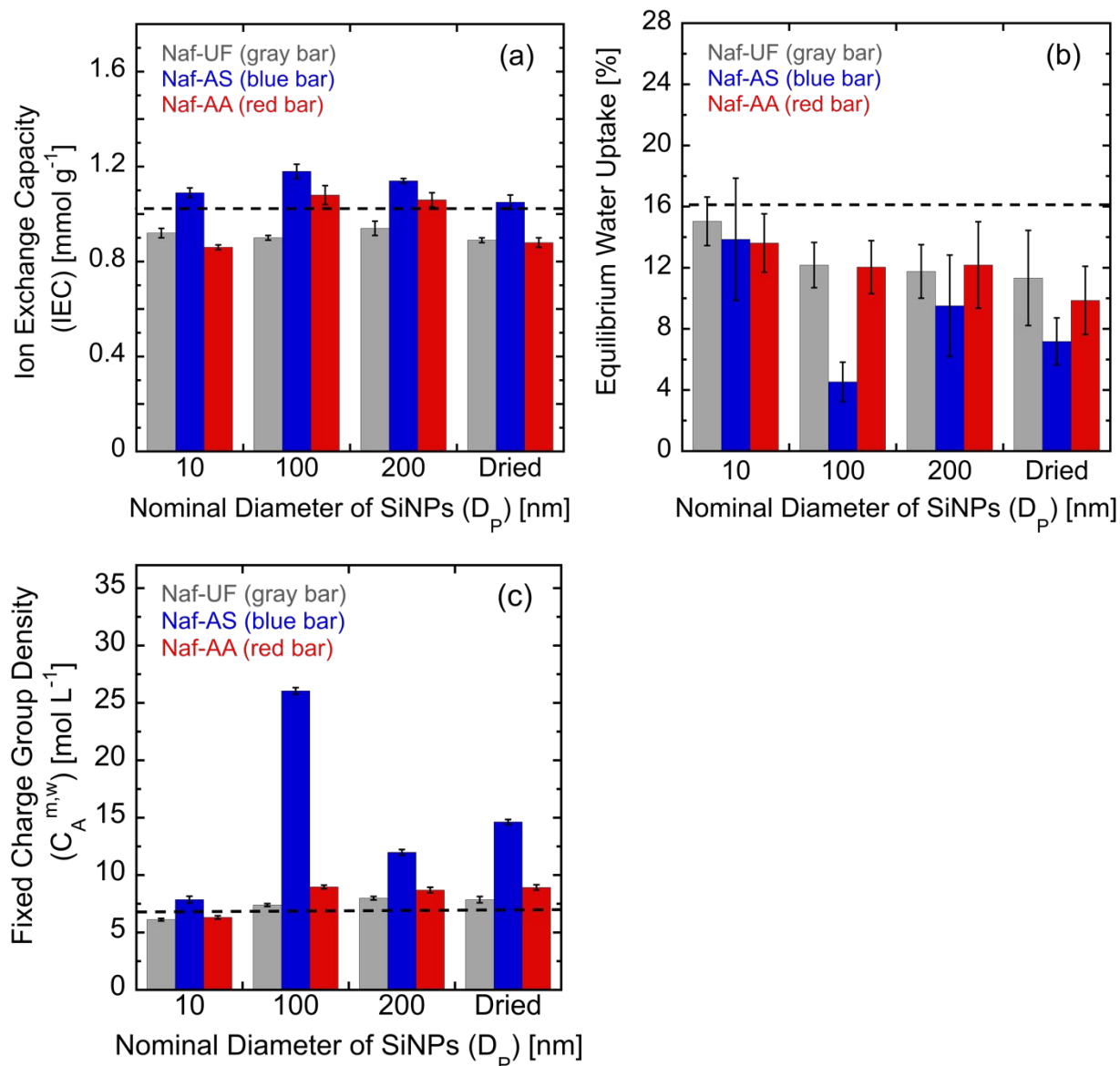
Figure 3. (a) Ion exchange capacity (IEC), (b) equilibrium water uptake, and (c) fixed charge group density for Nafion nanocomposites containing a mass fraction of 5% SiNPs with varying nominal diameters and surface functionalities. Ionomer membranes containing UF-SiNP, AS-SiNP, and AA-SiNP are shown in solid gray, blue, and red bars, respectively. The dashed black lines represents the calculated average IEC and equilibrium water uptake of Pristine–Naf. The error bars in each figure represent the standard deviation of the average value, which was calculated from experiments on at least three separate membranes.

thus, the water uptake   properties directly impact the proton conductivity of the ionomer

nanocomposites. Hence, IEC and water uptake are discussed together. In principle, changes to

the IEC and water uptake of an ionomer can significantly alter vanadyl ion (VO^{2+}) permeability, as it is   well known that the concentration of charged groups strongly influences sorption and transport of ions in charged polymers.[49–51,52,53]

As shown in Figure 3a, the IECs for ionomers containing UF–SiNP were independent of NP size, where no statistically significant differences in IECs amoung membranes in this series were observed. Further, excluding Naf–UF–200, the IEC values for these membranes are lower than that of Pristine–Naf. Similarly, the IECs of membranes containing AA–SiNP are either lower than or show no statistical difference when compared to Pristine–Naf. In contrast, Naf – AS membranes exhibited IECs that were greater than that of Pristine–Naf, where the highest IEC was measured for Naf–AS–100 and Naf–AS–200. Interestingly, the IEC valus for the various membranes within each series do not appear to correlate with the measured VO^{2+} permeabilities. For example, the IECs of Naf–AS membranes are greater than that of Pristine–Naf and yet these membranes exhibit the highest VO^{2+} permeabilities when comparing amoung the various series. In contrast, two of the lowest permeabilities were exhibited for Naf–AA–100 and Naf–AA–200, though the calculated IECs of these membranes are not statistically different than that of Pristine–Naf.

Along with IEC, the equilibrium water uptake for each membrane was measured and the results are summarized in Figure 3b. In general, ss seen in Figure 3b, the introduction of SiNPs leads to a reduction in equilibrium water uptake for the ionomer nanocomposites, with the exception of membranes containing 10 nm SiNPs, where no statistically significant ddifferences between the water uptake of these membranes and Pristine–Naf were observed. Similar to what was seen with the IEC values, there is no decernable correlation between the water uptakes and VO^{2+} permeabilities of the various membranes with each series. This is especially true for

31

membranes containing UF–SiNP and AS–SiNP, where higher VO^{2+} permeabilities were observed for membranes with equilibrium water uptake values lower than that of Pristine–Naf, though these differences in water uptake are only on the order of a couple of percentage points. In addition to viewing IEC and water uptake individually, the ratio of IEC and water uptake provides another useful parameter, the fixed charge group density $C_A^{m,w}$, which represents the concentration of fixed charge groups in the ionomer (i.e., mmol of fixed charge groups per mL of sorbed water; here A is SO_3^-). The fixed charge group density of each ionomer nanocomposite can be computed via the following equation: $C_{SO_3^-}^{m,w} = (IEC \times \rho_w)/w_u$, where w_u is the water uptake (in grams of water per gram of dry polymer) and ρ_w is the density of water (taken as 1 g cm^{-3}).[48] The parameter $C_{SO_3^-}^{m,w}$ is a more accurate representation of the electrostatic environment the diffusing ions experience inside the ionomer, and when taken in conjunction with the total ion concentration of the adjacent solution C_T^s, can provide insight into the impact of Donnan exclusion (repulsion) on the permeability of ions through the membrane.

Traditionally, Donnan theory has been utilized to provide insight into the impact of IEC values on ion transport, or the partitioning of ions into (and out of) the ionomer.[54–56] For electrostatic repulsion of counter ions into the ionomer to occur (or restriction of the desorption of co-ions to occur), the total ion concentration of the adjacent solution must be less than the fixed charge density of the ionomer − i.e., $C_T^s < C_{SO_3^-}^{m,w}$ − such that the fixed charges in the membrane are not sufficiently screened by the sorbed counter ions. At high enough ion concentrations in the external solution, the environment inside the membrane and that of the contiguous solution become thermodynamically similar. Using the information from Figures 3a and 3b, $C_{SO_3^-}^{m,w}$ was calculated for Nafion and each Nafion nanocomposite. The results have been summarized in Figure 3c. For the electrolyte concentrations utilized in permeation experiments,

we calculate a value of total ion concentration in the solution $C_T^s = C_{SO_3^-}^s = C_{VO^{2+},H^+}^s \approx 5$ mol L^{-1} (recalling that the donating reservoir contains 1.5 mol L^{-1} VOSO$_4$ in 3.0 mol L^{-1} H$_2$SO$_4$).

As seen from Figure 3c, the fixed charge densities of all of the membranes is greater than 5 mol of ions per L of sorbed water, though most fall with a narrow range of approximately (6 to 8) moles of ions per L of sorbed water. Notable exceptions to this are Naf–AS–100, Naf–AS–200, and Naf–AS–Dried, which all had $C_{SO_3^-}^{m,w}$ values greater than 10, with Naf–AS–100 exhibiting a value as high as 25 mol of ions per L of sorbed water. These high values suggest that the electrostatic potential between the ionomer nanocomposites and the external electrolyte solutions could play a role in governing ion transport through these membranes, though no correlation between the elevated values of $C_{SO_3^-}^{m,w}$ and vanadyl ion permeabilities for these membranes was observed. However, as the total ion concentration of the membrane-adjacent donating solution ($C_T^s \approx 5$ mol L^{-1}) is close to or similar to the $C_{SO_3^-}^{m,w}$ of most of the ionomer membranes, the impact of Donnan exclusion/repulsion on ion transport in these membranes would be minimal due to a sufficient amount of ions in membrane (from the external solution) that effectively screen the fixed charges of the membrane. It is clear from these calculations that a complete understanding of the effect of particle size on the performance of these PFSA ionomer nanocomposites cannot be solely attributed to changes to the IEC and water uptake of these membranes.

3.2. Proton Conductivity and Ion Selectivity

To gain additional insight into the impact of SiNP size and surface functionality on ion transport, the proton conductivity, and in turn the proton selectivity, of each membrane was calculated. Figure 4 shows both the proton conductivity (Figure 4a) and the ion selectivity (Figure 4b) of
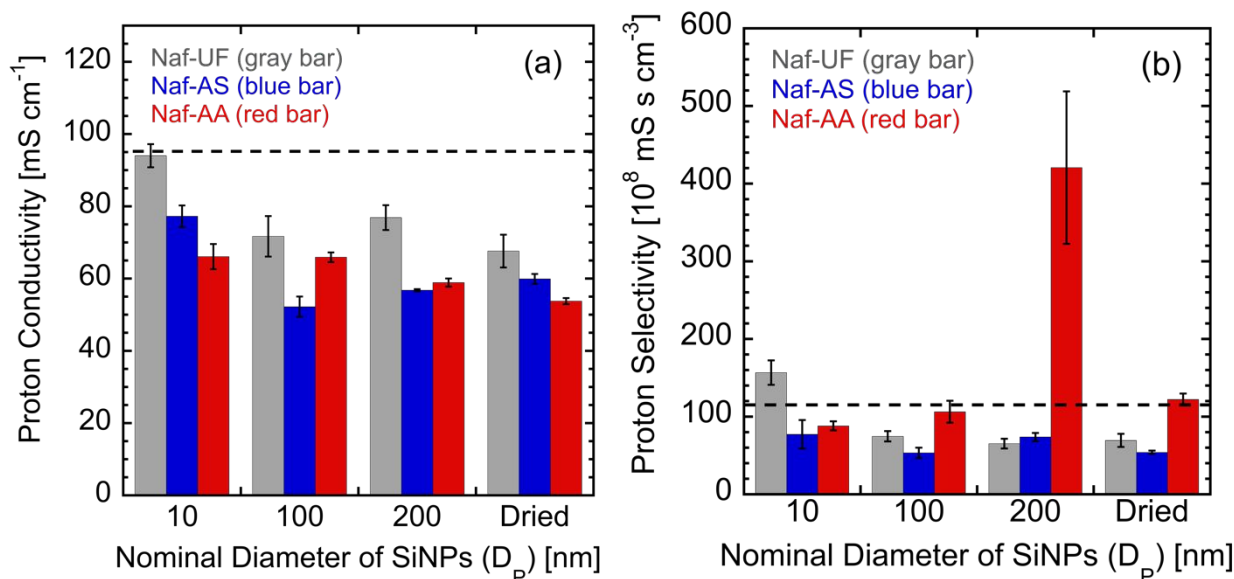
Figure 4. (a) Proton conductivity of Nafion nanocomposites. The dashed black line represents the calculated average proton conductivity of Pristine–Naf. (b) Proton selectivity (i.e., proton conductivity divided by vanadyl ion permeability) of Nafion nanocomposites. The dashed black line represents the calculated average ion selectivity of Pristine–Naf. Error bars in each plot represent the standard deviation of the average value, which was calculated from experiments on at least three separated membranes.

pristine Nafion and Nafion nanocomposites. Here, proton selectivity was calculated as the proton conductivity (in mS cm^{-1}) divided by the vanadyl ion permeability (in cm^2 s^{-1}). For reference, the average proton conductivity (95.9 ± 6.5 mS cm^{-1}) and proton selectivity ((118.5 ± 15.4) $\times$ 10^8 mS s cm^{-3}) of Pristine–Naf is represented by the dashed black lines in Figures 4a and 4b, respectively. As seen from Figure 4a, all nanocomposite membranes, except those containing 10 nm UF–SiNP, exhibited proton conductivities lower than that of Pristine–Naf. For Naf–UF–10, the proton conductivity was not statistically different than that of Pristine–Naf. Further, within a particular nominal diameter group, ionomers containing UF–SiNP always exhibited higher proton conductivites than those containing either AS-SiNP or AA-SiNP, with the exception of Naf–AA–100, where no statistical difference in proton conductivity between Naf–AA–100 and Naf–UF–100 is observed. The proton conductivity of membranes containing UF–SiNP is seen to

drop from $\approx$ 95 mS cm^{-1} to $\approx$ 70 mS cm^{-1} when the size of the NPs is >10 nm. When comparing this trend with that observed for VO^{2+} permeability, we observe the opposite behavior, where the VO^{2+} permeability is seen to increase with increasing SiNP size, where the lowest permeability is observed for Naf–UF–10.

While high proton conductivity is desired for energy storage and delivery technologies, it is also important to characterize the proton selectivity of each ionomer nanocomposite as this parameter provides insight into the potential trade-off between the desired low vanadium ion permeability and high proton conductivity. As seen in Figure 4b, there are only four membranes with proton selectivities greater than or equal to that of Pristine–Naf – Naf–UF–10 and composite membranes containing AA–SiNP with nominal diameters >10 nm. Specifically, Naf–UF–10 and Naf–AA–200 exhibited proton selectivities greater than that of Pristine–Naf, while the proton selectivies of Naf–AA–100 and Naf–AA–Dried were not statistically different from that of Pristine–Naf. Most notably, Naf–AA–200 exhibited an proton selectivity four-fold greater than that of Pristine–Naf. Noting that both the VO^{2+} permeability and the proton conductivity decrease with the introduction of 200 nm AA–SiNP, we posit that the electrostatic interactions between the sulfonic acid groups (of Nafion) and the protonated amine groups (of the functionalized NPs) lead to either a decrease in the size/spacing of the ionic channels or an increase in the tortuosity of the ionic channels in the membrane (or some combination of both). This decrease in size more heavily impacts vanadyl ion transport (which is believed to primarily occur through a "vehicular transport" mechanism – i.e., through the center of the ion channels as hydrated ions) as compared to proton conductivity (which is believe to primariliy occur through a "proton hopping" mechanism – i.e., along the walls of the ion channels). However, little correlation is observed between proton conductivity and IEC values (Figure 4a vs. Figure 3a),

highlighting why IEC cannot be used alone as a predicter of ion transport rates in these PFSA ionomer membranes. To help provide further insight into the observed changes in ion selectivity with SiNP size and surface chemistry, the NP dispersion states for each of the composite membranes were imaged using electron and optical microscopy.

3.3. Silica Nanoparticle (SiNP) Dispersion State

Transmission electron microscopy (TEM) was utilized to image the SiNP dispersion states within the PFSA nanocomposites containing SiNPs with varying surface chemistry and nominal diameters of 100 nm and 200 nm. These TEM images are presented in the first two columns of Figure 5. For nanocomposites containing Dried NPs (i.e., SiNPs (or particles) with nominal diameters of >1000 nm), the particles were too large to image via TEM, and optical microscopy, equipped with a polarized lens, was utilized to characterize the SiNP dispersion states of these membranes. The images obtained by optical microscopy are presented in the third column (i.e., far right column) of Figure 5. Note, TEM images of nanocomposite membranes containing 10 nm particles have been previously published and therefore, are not presented in Figure 5.[28]

As mentioned in the last section, the sizes of the SiNPs listed in Table 1 are nominal sizes, which come from a visual inspection of the electron and optical microscopy images presented in Figure 5. We point this out to the reader, as in some cases, these nominal sizes differed drastically from the sizes listed by the manufacturer. This was most notable in membranes containing SiNPs with a nominal size of 100 nm (i.e., TEM images located in the first column of Figure 5). First, we observe the presence of significantly smaller particles, on the order of 5 nm to 20 nm in diameter, in Naf–AA–100 (Figure 5g), which are not observed in either Naf–UF–100 or Naf–AS–100 (Figures 5a and 5d, respectively), where the average sizes of UF-100 and AS-
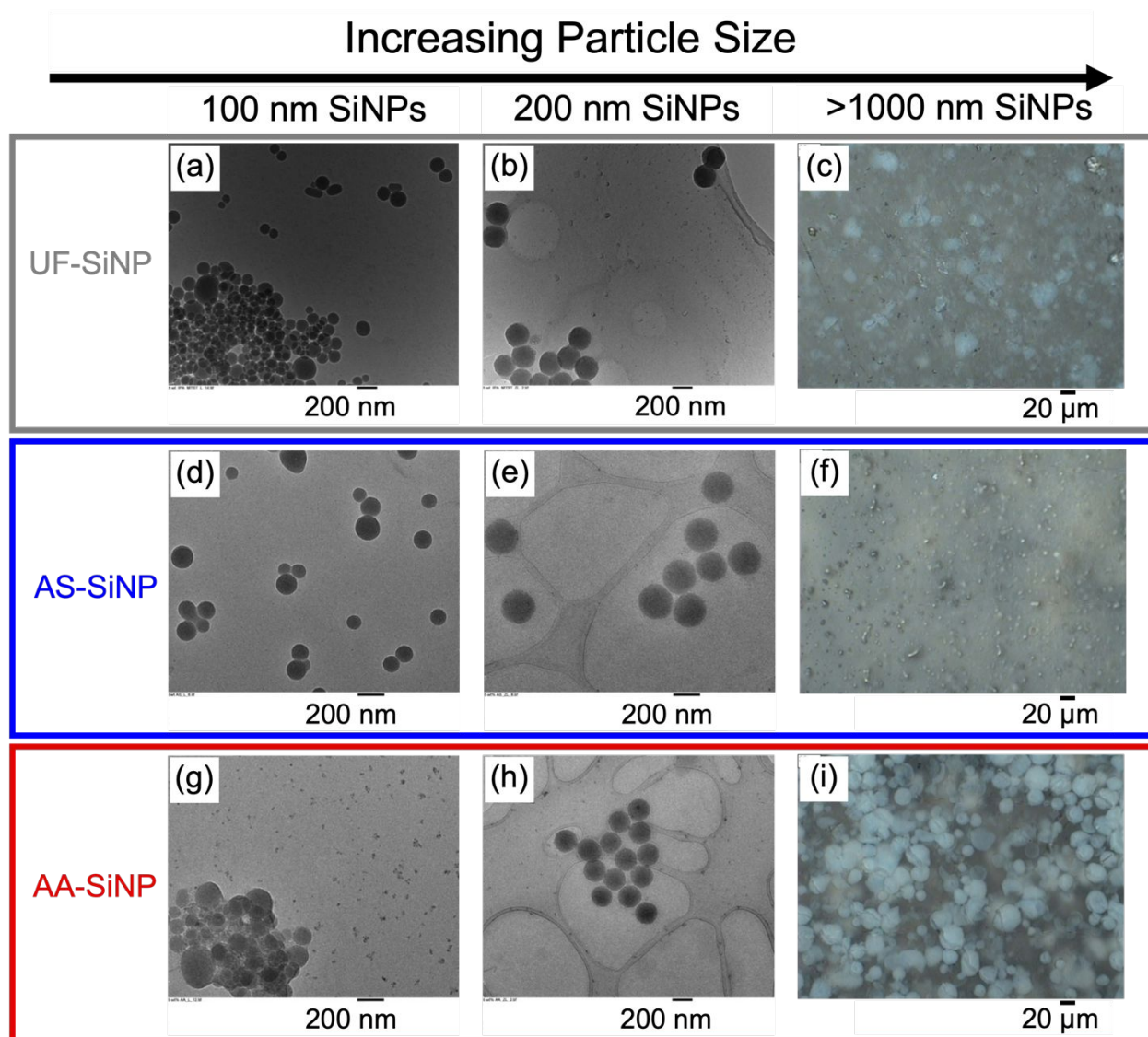
Figure 5. (a, b, d, e, g, h; first two columns) Transmission electron and (c, f, i; far right column) optical microscopy images of PFSA nanocomposite membranes containing a mass fraction of 5% SiNPs with various surface functionalizations. The microscopy images are organized in rows according to their surface chemistry, where top, middle, and bottom rows represent Naf–UF (outlined in gray), Naf–AS (outlined in blue), and Naf–AA membranes (outlined in red), respectively. As seen at the top of the images, the images are organized in columns according to the sizes of the SiNPs, which increase from left to right. Note, the scale bars for all TEM images are 200 nm, while the scale bars for all optical microscopy images are 20 μm. The optical microscopy images were obtained with a polarized lens.

100 particles are approximately 100 nm. Furthermore, the NP dispersion states among these three membranes are drastically different, where signficant aggregates are observed in both Naf–UF–100 and Naf–AA–100. These results are almost analogous to previous results obtained from

our group, where 'diffuse' and 'tighter' aggregations of SiNPs were observed for Naf–UF–10 and Naf–AA–10, respectively. In contrast, at 100 nm, a relatively uniform dispersion was seen for Naf–AS–100,[27,28] which is also analogous to prior our results on Naf–AS–10, where TEM images showed uniform NP dispersion states for PFSA ionomers containing sulfonic acid-functionalized SiNPs. For ionomer membranes containing SiNPs with a nominal size of 200 nm, both the NP sizes (and distribution of sizes) and the NP dispersion state were similar across all membranes, with NPs in Naf–UF–200, Naf–AS–200, and Naf–AA–200, ranging from approximately 200 nm to 230 nm in diameter. Note, the web-like structure observed in the background of these images arises from the lacey carbon of the TEM grid support and is not a feature of the ionomer nanocomposite. As seen in Figures 5b, 5e, and 5h, the all of the NPs exhibit diffuse clustering, though the degree of clustering (i.e., 'buffer zone' between individual NPs) appears to vary with surface chemistry. Specifically, the NP aggregates become more diffuse as follows: AS–200 > AA–200 > UF–200. Lastly, optical microscopy images of ionomer membranes containing a mass fraction of 5% Dried SiNPs showed particles with diameters ranging from approximately 5 μm to 30 μm, for all functionalities.

Interestingly, UF–SiNP and AA–SiNP tended to aggregate regardless of size, with the highest degree of aggregation observed in ionomer membranes containing AA–SiNP. The increase in VO^{2+} permeability with increasing UF–SiNP size is not as clearly described by the dispersion of the particles, though it is obvious that clusters (or aggregates) of particles form at all nominal sizes, where the size of these aggregates shows no discernable trend with respect to particle size. Significant aggregation of AA–SiNP was observed for all particle sizes, though the highest degree of aggregation was seen in nanocomposites containing either 10 nm or > 1 μm

NPs. Most notably, the aggregates within Naf–AA–Dried span across the entire optical microscopy image, where some larger aggregates appear to be on the order of tens of microns.

As previously observed by our group, the presence and degree of SiNP aggregation appears to directly affect the VO^{2+} permeability and proton conductivity, especially for ionomers containing SiNPs with amine-functionality.[28] The permeation data for this series of membranes suggests that an optimal SiNP aggregate size exists for these PFSA composite membranes, where in our previous work, aggregates on the order of 500 nm in size were also observed in Naf–AA–10. Overall, it is clear that the size of the nanoparticles, whether that be with respect to the presence of micron-sized particles or with respect to large NP aggregates, results in a reduction in the VO^{2+} permeability for Naf–AA, when compared not only to Pristine–Naf, but also to Naf–UF and Naf–AS. In contrast, AS–SiNP, regardless of size, are better dispersed within the PFSA ionomer. The lack of significant aggregation in Naf–AS membranes – i.e., a more uniforn SiNP dispersion state – appears to be captured in both the VO^{2+} permeability and proton conducitivty data, where a relatively constant value of proton selectivity for this series of membranes is observed.

3.4. Composite Membrane Morphology

In this section, SANS experiments were performed on hydrated Nafion and Nafion nanocomposite membranes to elucidate the relationship between the ion selectivity, SiNP dispersion state, and the nanostructure of the PFSA ionomer nanocomposites. All SANS measurements were performed on membranes hydrated (i.e., equilibrated) in water (i.e., 100% H_2O) at 25 °C. The SANS curve for hydrated Pristine–Naf is shown in Figure 6. Although these data have been previously published by our group,[26] they have been included in the current
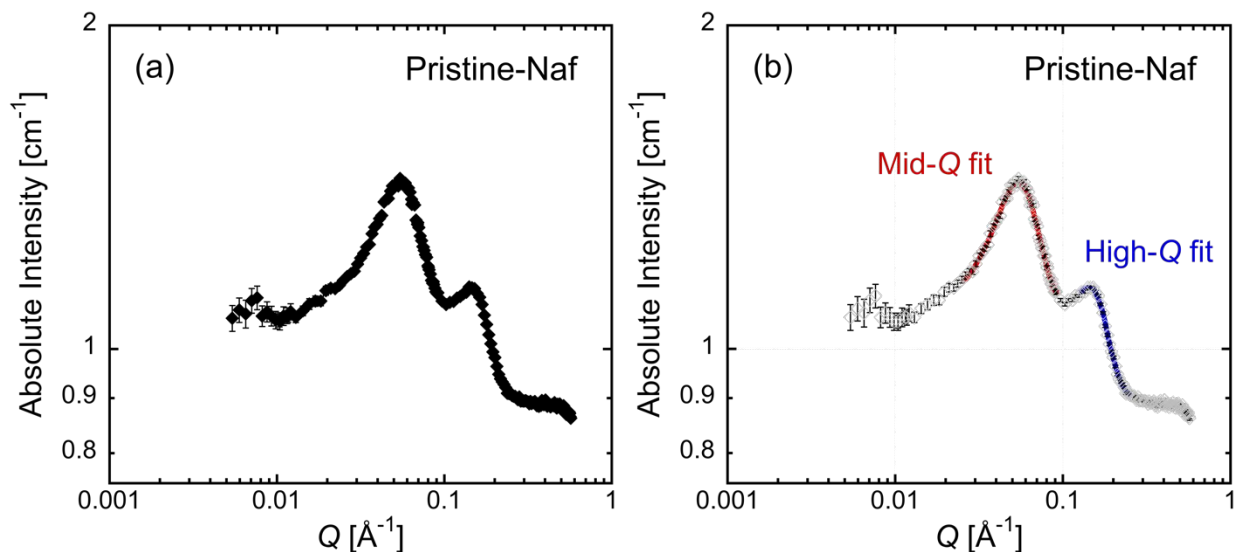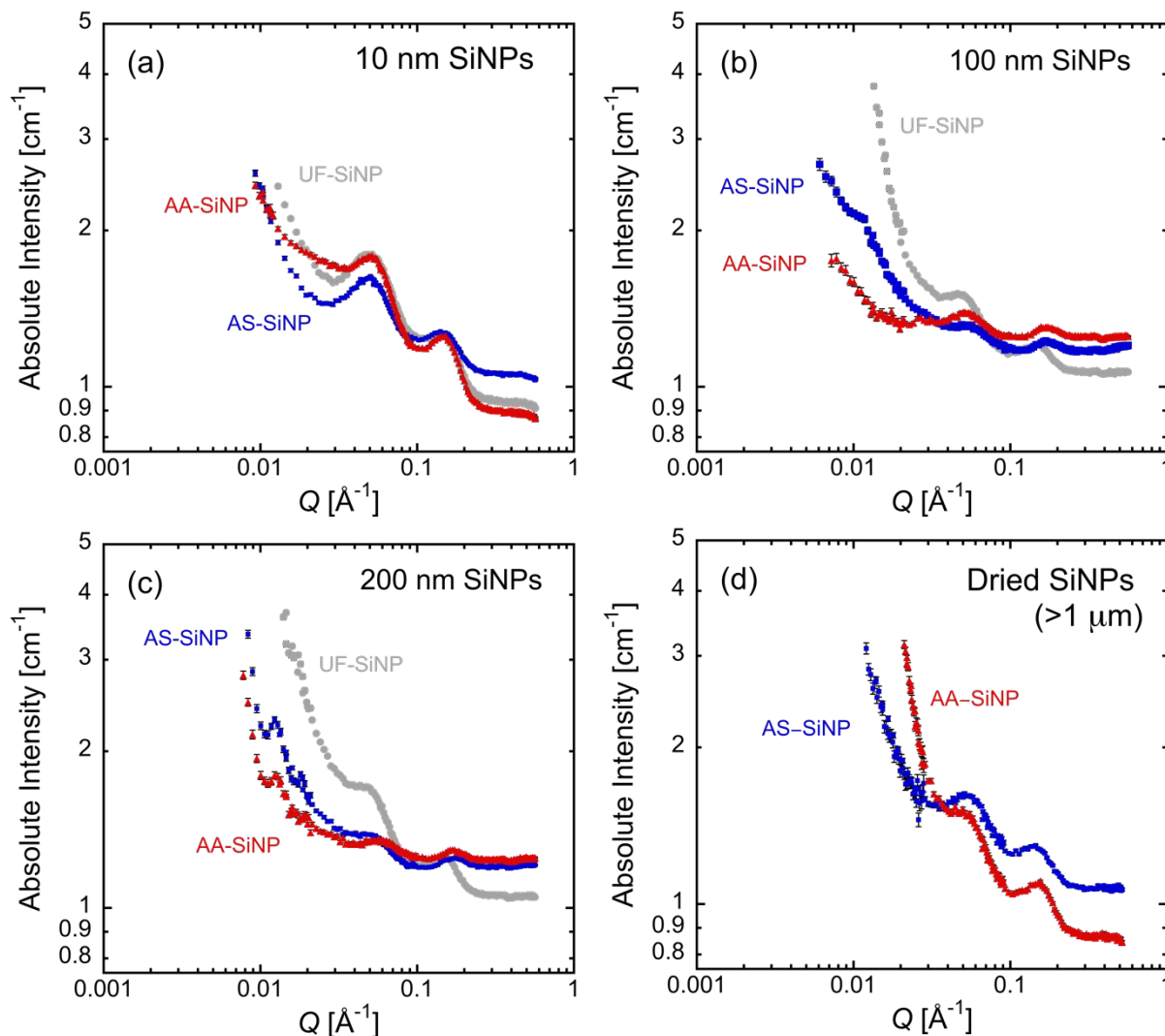
Figure 6. Small-angle neutron scattering (SANS) curve for hydrated pristine Nafion. (b) Gaussin fit of the mid-Q (hydrophobic; solid red line) and high-Q (hydrophilic; solid blue line) peaks of pristine Nafion. All membranes were hydrated in 100% H_2O for at least 24 h prior to SANS experiments. The error bars on the SANS data for each membrane represent the standard deviation in calculated intensities. Note, the scattering data shown in (a) and (b) have been previously published.[28]

manuscript for ease of comparison for the reader. While the exact nanostructure of Nafion is still debated today, one of the most accepted structures is known as the "cluster network model", which describes an interconnected network of spherical ionic domains surrounded by the hydrophobic perfluoronated backbone, which provides the mechanical support for the ionomer membrane.[4,7] As seen in Figure 6a, the SANS curve for hydrated Pristine–Naf contains two characteristic scattering peaks, one in the high-Q region at $Q \approx 0.144$ Å^{-1} and one in the mid-Q region at $Q \approx 0.055$ Å^{-1}, that are directly correlated to the periodic spacing of the hydrophilic and hydrophobic domains of the ionomer, respectively.[5,26] Henceforth, the high-Q and mid-Q scattering peaks will be referred to as the hydrophilic and hydrophobic peaks, respectively. Figure 6b shows the same scattering curve, where the hydrophobic (solid red line) and hydrophilic (solid blue line) peaks have been regressed to a Gaussian model. More details

regarding the results of this regression for all of the membranes will be provided later in this section.

Figure 7. Small-angle neutron scattering (SANS) curves for hydrated (a) pristine Nafion and Nafion nanocomposites containing a mass fraction of 5% SiNPs with various surface functionalities and nominal diameters of (b) 10 nm, (c) 100 nm, and (d) 200 nm. Specifically, the SANS curves for Pristine–Naf, Naf–UF, Naf–AA, and Naf–AS are shown in solid black diamonds, gray circles, red triangles, and blue squares, respectively. All membranes were hydrated in 100% H_2O for at least 24 h prior to SANS experiments. The error bars on the SANS data for each membrane represent the standard deviation in calculated intensities.Note, the scattering data shown in (a) and (b) have been previously published.[28]

Figure 7 shows the SANS curve for hydrated Nafion nanocomposites. Specifically, the scattering curves for ionomers containing a mass fraction of 5% SiNPs with varying surface functionalitiy and nominal diameters of 10 nm, 100 nm, 200 nm, >1 μm are shown in Figures 7a, 7b, 7c, and 7d, respectively. Note, the SANS curves shown in Figure 7 have been truncated at

low-Q. That is, a portion of the low-Q data has been excluded from these figures as the absolute intensity of the lower Q data points visually obscures the changes to the hydrophobic and hydrophilic peaks. The full scattering curves can be found in the ESI[†] (Figures S1-S4). Also note, while the scattering curves shown in Figure 7a have been previously published by our group, it has been included in this manuscript for ease of comparison for the reader. Further, the scattering data for membranes containing UF-SiNP has been previously published by our group. As the actual curve did not significantly add to the discussion of the current data, it has been omitted from from Figure 7d.[6] Upon an initial visual inspection of the scattering curves shown in Figures 7b-d, it appears that the hydrophobic peaks have shifted to lower Q values (i.e., large d-spacing), while the hydrophilic peak locations have remained unchanged or shifted to higher Q values (i.e., smaller d-spacing) when compared to Pristine–Naf. In addition, a low-Q upturn in the SANS data, which is not present in the Pristine-Naf case, can be observed for all ionomer nanocomposites. This upturn has previously been attributed to aggregation (or agglomeration) of the SiNPs.[48]

First, focusing our attention on this low-Q upturn, we observe a trend with SiNP surface functionalization and the Q value at which the low-Q upturn begins. Specifically, the low-Q upturn is seen to begin at higher Q values for membranes containing UF-SiNP, followed by those containing AS–SiNP, and finally by those containing AA–SiNP. This trend follows what is observed in the TEM images, where the largest SiNPs aggregates were observed for membranes containing AA–SiNPs. The exception to this trend is seen for membranes containing "Dried" SiNPs (Figure 7d), where the low-Q upturn for Naf–AA–Dried is seen to occur at a slightly higher Q value than Naf–AS–Dried. Next, looking at the scattering curves for membranes containing 100 nm SiNPs (Figure 7b), an additional inflection in scattering curve of Naf–AS–

100 (at $Q \approx 0.01$ Å^{-1}) is observed. In fact, when looking at the full scattering curves (see Figures S1-S4), an inflection in the low-Q data is seen to occur for all of these membranes. Furthermore, this inflection becomes more apparent in all of the truncated scattering curves when the SiNP nominal size is increased from 100 nm to 200 nm (Figure 7b vs. Figure 7c). This inflection in the scattering data may be a fringe from the form factor of the spherical SiNPs or may be indicative of large aggregates of the SiNPs. The authors attempted to gather more quantitative information from this feature in the scattering curve by fitting the low-Q data, for both 100 nm and 200 nm SiNPs, with a spherical form factor. While the model provided reasonable fits to the scattering data (i.e., the sum of squared error between the model and the scattering data were low), the physical parameters returned (e.g., radius of particle) were not physically realistic for the systems. This discrepancy between the model parameters and the nominal particle sizes observed in the TEM images may be due to scattering features of these larger particles existing outside the Q-window of this particular SANS instrument. While outside the scope of this investigation, complementary small-angle X-ray or ultra small-angle X-ray/neutron scattering may be useful in elucidating the origins of this low-Q feature.

To confirm the shifts in the hydrophobic and hydrophilic peaks observed by visual inspection of the scattering curves, a quantitative characterization of the peak locations was performed. According to the Bragg approximation, the wave vector of a peak q^* can be correlated to the Bragg d-spacing of each feature ($\approx 2\pi/q^*$). To determine the peak location (as well as the distribution width – i.e., standard deviation), both the hydrophobic and hydrophilic peaks were fit to a Gaussian model (see Figure 6b). This analysis was also applied to the hydrophobic and hydrophilic peaks for all the ionomer nanocomposites. A summary of the values for the d-spacing of each scattering peak and the spread (or breadth) of the peak for all of the ionomer

nanocomposites is provided in Figure 8. Specifically, the d-spacing (peak maximum) and
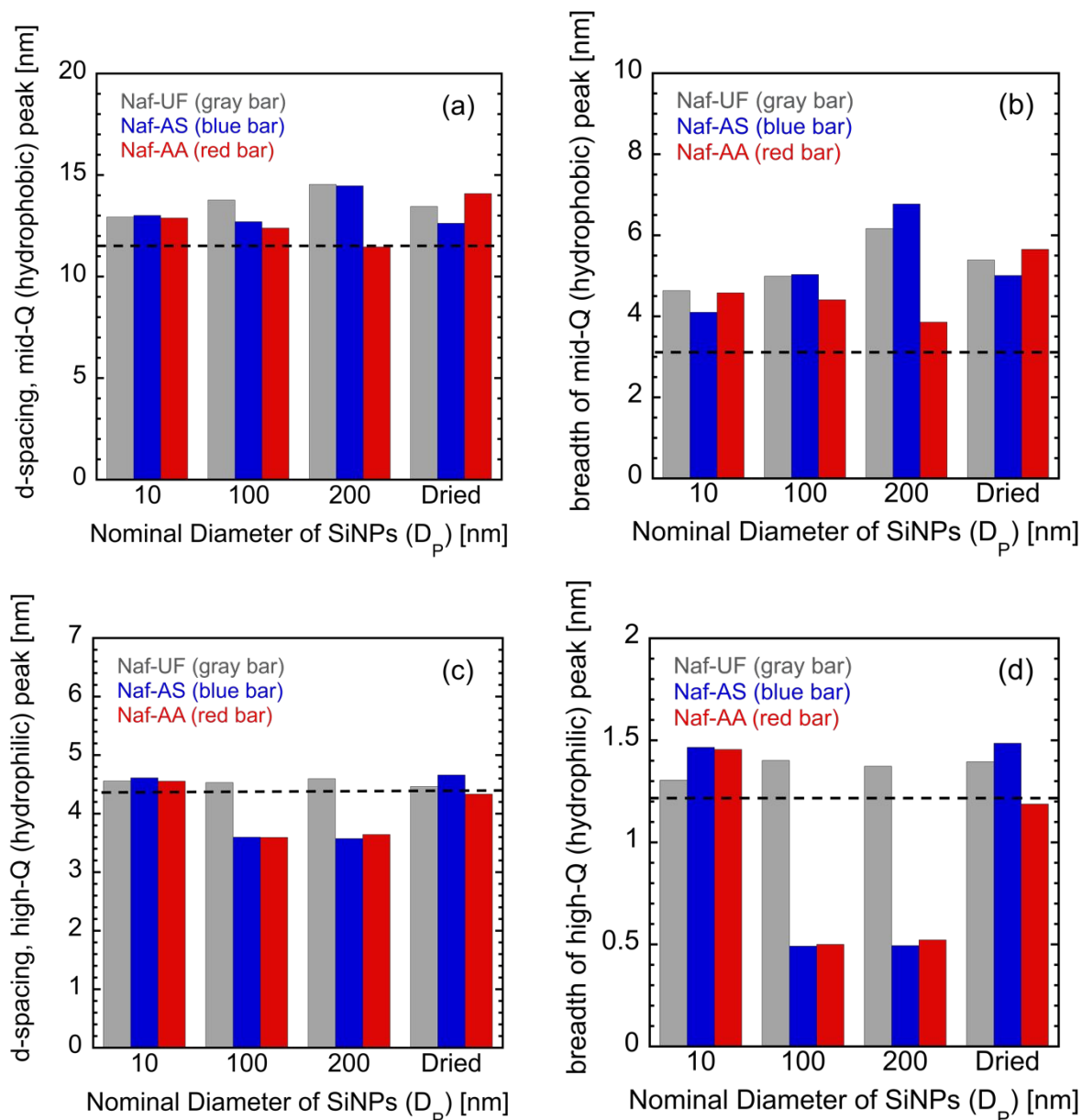
Figure 8. d-spacings (in nm) of the (a) mid-Q (hydrophobic) and (c) high-Q (hydrophilic) scattering data for Nafion and Nafion nanocomposites containing a mass fraction of 5 % unfunctionalized and functionalized SiNPs with nominal diameters ranging from 10 nm to >1 μm. Breadth of the (b) mid-Q (hydrophobic) and (d) high-Q (hydrophilic) correlation peaks, which was obtained from regression of a Gaussian model to the SANS curves. The dash line in each figure represents the value for Pristine–Naf (no SiNPs).

breadth of the correlation peak obtained from fitting the the mid-Q (hydrophobic) peak are

shown in Figures 8a and 8b, respectively, while the d- spacing (peak maximum) and breadth of

the   correlation peak obtained from fitting the the high-Q (hydrophilic) peak are shown in

Figures 8c and 8d, respectively. For reference, the d-spacings for the mid-Q (11.5 nm) and high-

Q (4.5 nm) peaks for Pristine–Naf are represented by the dashed black lines in Figures 8a and 8c,

respectively. The visual changes to the peak locations and breadth in the SANS curves are

verified by the peak locations obtained through fitting of these peaks to a Gaussian model. As

seen in Figure 8a, the introduction of SiNPs results in an increase in the periodic spacing of the

hydrophobic domains of the nanocomposites, irrespective of the nominal diameter and surface

chemistry of the SiNP. Futher, it can be seen from figure 8b that the breadth of the hydrophobic

peak increases (in some cases significantly) when compared to Pristine–Naf, where the largest

peak breadth is observed for Naf–AS–200 (≈ 7 nm vs. ≈ 3 nm). These data show that the

introduction of SiNPs not only alters the spacing of the hydrophobic domains but also the

distribution in this spacing (i.e., dispersity).

Next, the impact of SiNP size and surface functionality on the periodic spacing of the ionic

domains is summarized in Figure 8c. Surprisingly, there is little correlation observed between the

spacing of the ionic domains and the proton selectivity of each membrane (Figure 8c vs. Figure

4b). For example, for Naf–AA–200, which exhibited a four-fold increase in protron selectivity,

we observe a decrease in the periodic spacing of the ionic domains. However, we also observe a

decrease in the spacing of the ionic domains for Naf–AA–100, which exhibited almost no change

in proton selectivity when compared to Pristine–Naf. Further, as seen from Figure 8c, little

change in the spacing of the ionic domains is observed for most of the ionomer nanocomposites

studied, where for example, the spacing of the ionic domains for membranes containing UF-

SiNPs was equivalent to Pristine–Naf at all SiNP nominal diameters. With the introduction of

functionalized particles with stronger surface charge than UF–SiNP (which are near their

isoelectric point at the pH utilized in solution casting), it follows that as the size of the NPs is increased, the spacings of the ionic domains are reduced for both AS–SiNP and AA–SiNP, as the stronger electrostatic interactions of the ionic groups with the surface charge of both SiNPs force the ionic domains to reorganize. In this case, the reorganization results in a tighter periodic spacing of this ionic transport channels. However, it is clear that the absolute value of the spacings of these domains cannot alone be used to predict the VO^{2+} permeability.

In contrast to what was observed with the hydrophobic peak, as seen in Figure 8d, the breadth of the hydrophilic peak is seen to both decrease and increase with SiNP size and surface functionalization. Specifically, the breadth of this peak is seen to increase for all membranes except those containing 100 nm and 200 nm AS–SiNP and AA–SiNP, where for these membranes, the peak breadth was ≈ 0.5 nm vs. ≈ 1.25 nm for pristine Nafion. This result is quite interesting as the vanadyl ion permeability for membranes containing AS–SiNP was similar to (or slightly higher than) Pristine–Naf, while the vanadyl ion permeabilities for membranes containing AA–SiNP were signficiantly lower than that of Pristine–Naf. While it is traditionally believed that water and ion transport in these PFSA ionomers is dictated by the ionic network (i.e., spacing of ionic domains) of the polymer, these results highlight that changes to the ionomer nanostructure do not necessarily correlate with the observed changes in ion transport within these ionomer nanocomposites. These results are similar to those recently reported on Nafion membranes containing hydrophobically-functionalized SiNPs, where the periodic spacing of the hydrophobic domains was seen to be more significantly impacted than the hydrophilic (ionic) domains, though almost a two-orders of magnitude increase in ion selectivity was observed.[57] It is important to note that while changes in the tortuosity of the ionic network cannot be captured via neutron scattering, one would expect that both the SiNP size and surface

chemistry may alter the tortuosity of the ionic domains. Changes to the tortuosity of the transport channels could help better explain the observed changes in both VO^{2+} permeability and proton conductivity.

## 3.5. Comparison of Pre-functionalized and In-house-functionalized SiNPs with Amine-Functionality

Before continuing, it should be noted that up to this point, all data that have been presented for Naf–AA–Dried, have come from PFSA ionomer composites fabricated with SiNPs that were pre-functionalized with an amine surface chemistry (i.e., the SiNPs were functionalized prior to purchase and used 'as is'). To investigate whether better VO^{2+} crossover performance could be achieved by performing the amine functionalization 'in-house' on UF–Dried, functionalization of these particles was performed in the manner previously described. Note, the purchased, pre-functionalized NPs have been previously denoted as AA–Dried, while the in-house amine-functionalized dried particles are denoted as AA–Dried(F). Following functionalization, the two different particles were incorporated into PFSA ionomers, and VO^{2+} permeability experiments, IEC measurements, and optical microscopy were performed on these membranes. In addition, to obtain a rough estimage of the average particle size, DLS measurements were performed to obtain the hydrodynamic diameter of each of the dried amine-functionalized particles. The results of this analysis are presented in Table 2.

Table 2. Summary of vanadyl ion permeabilities and IECs for PFSA ionomers containing a mass fraction of 5% Dried, amine-functionalized particles that were either purchased pre-functionalized or were functionalized in-house. The hydrodynamic diameter for each set of particles, obtained from DLS measurements, is also provided. Note, the error for each reported value represents the standard deviation of the calculated average, which was calculated from experiments on at least three separated membranes.

| PFSA Ionomer Membrane	Vanadium Ion Permeability $(10^{-8} \text{ cm}^2 \cdot \text{s}^{-1})$	IEC $(\text{mmol} \cdot \text{g}^{-1})$	Hydrodynamic Diameter of Particles (nm)
Naf–AA–Dried	0.44 ± 0.02	0.92 ± 0.02	Outside of range of DLS
Naf–AA–Dried(F)	0.46 ± 0.01	0.88 ± 0.02	5600

A

s seen in Table 2, both the VO^{2+} permeabilities and the IECs for Naf-AA-Dried and Naf-AA-Dried(F) are within error of each other. However, as seen from the last colum in Table 2, the hydrodynamic diameters of the two particles are quite different. As noted, the AA–Dried particles could not be accurately analyzed by the Zetasizer DLS, which should be capable of
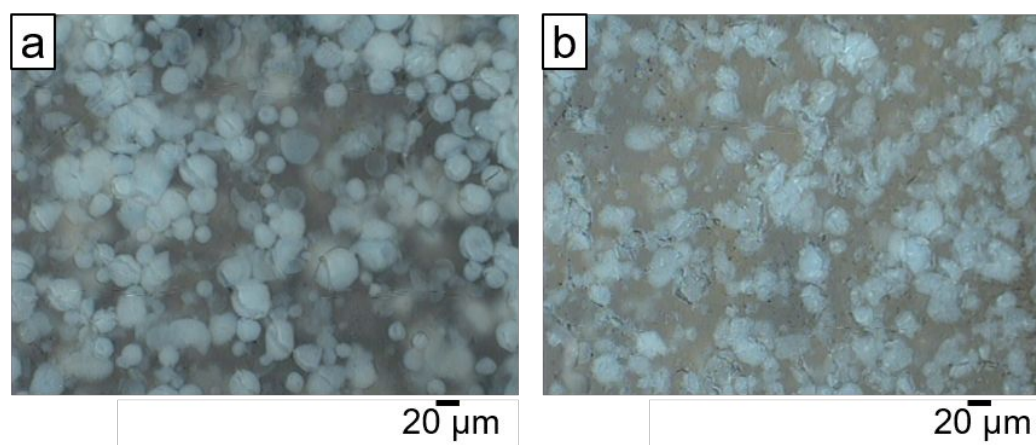
Figure 9. Optical microscopy images of PFSA ionomers containing a mass fraction of 5 % dried, amine-functionalized particles that were (a) purchased pre-functionalized (Naf–AA–Dried) or (b) functionalized in-house (Naf–AA–Dried(F)). Note, the image shown in (a) is identical to the image shown in Figure 4i. It has been included here for direct comparison. The scale bars of all optical microscopy images are 20 µm, and all images were obtained using polarized lens.

characterizing particles with diameters up to 10 μm. Therefore, the average size of these particles must be at larger than 10 μm in diameter, which is at least twice the average size calculated for AA–Dried(F) particles. The difference in particle shape is clearly observed in Figure 9, where the optical micrographs of Naf–AA–Dried and Naf–AA–Dried(F) composite membranes are shown. The AA–Dried appear to be more spherical in shape, with the presence of large, single particles, whereas individual AA–Dried(F) particles are less defined and appear as larger aggregates of smaller particles. To uncover differences in nanostructure between Naf–AA–Dried and Naf–AA–Dried(F), hydrated SANS experiments were performed on the two different membranes, and the resulting scattering curves are presented in Figure 10. Overall, the SANS
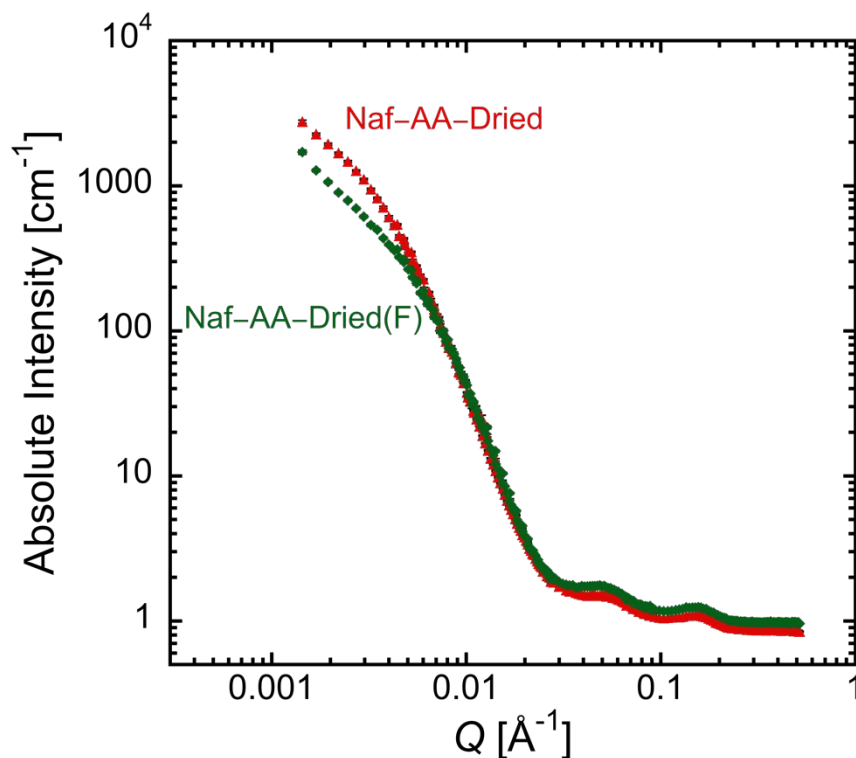
Figure 10. Small-angle neutron scattering (SANS) curves for hydrated Nafion nanocomposites containing a mass fraction of 5 % dried, amine-functionalized SiNPs that were either purchased pre-functionalized (Naf–AA–Dried; red triangles) or functionalized in-house (Naf–AA–Dried(F); green diamonds). Note, all membranes were hydrated in 100 % H_2O for at least 24 h prior to SANS experiments. The error bars on the SANS data for each membrane represent the standard deviation in calculated intensities.

curves for each composite membrane appear similar, and in fact, the spacings of the hydrophobic domains (13.6 nm and 14.0 nm for Naf–AA–Dried and Naf–AA–Dried(F), respectively) and hydrophilic domains (4.33 nm and 4.45 nm for Naf–AA–Dried and Naf–AA–Dried(F), respectively) are essentially identical between the two membranes. The biggest difference in the SANS curves of the two membranes appears in the lowest Q region of the scattering curve, where the slope of the scattering data for Naf–AA–Dried dec reases when compared to that for Naf–AA–Dried(F), though again, this difference is minimal.

CONCLUSIONS

Most notably, the lowest vanadyl ion permeability was observed for Naf–AA–200, where an over four-fold reduction in VO^{2+} permeability was achieved. While the proton conductivity of these membranes was seen to decrease by $\approx 30\%$, the proton selectivity of Naf–AA–200 was still the highest of all membranes investigated, exhibiting an ion selectivity that was approximately 400% higher than that of Pristine–Naf. Interestingly, the VO^{2+} permeability was seen to increase with increasing particle size (approximately doubling going from 10 nm to 200 nm) for Nafion membranes containing UF–SiNP. In contrast, Nafion membranes containing AS–SiNP exhibited VO^{2+} permeabilities that were either equal to or higher than that of Pristine–Naf, with no discernable correlation between the the nominal diameter and VO^{2+} permeability.

From TEM images, the NP dispersion state within the ionomer was seen to vary significantly with the NP surface chemistry. In addition, the SANS curves for the different series of nanocomposites were seen to vary drastically with both NP surface chemistry and size. Most notably, the low-Q region of the SANS curves were quite different, with the emergence of a new scattering peak – in some cases, multiple peaks (or shoulders) – which became markedly more

prominent when the nominal diameter of the SiNP was increased from 100 nm to 200 nm. We believe the low-Q features seen in the scattering curves for ionomers containing 100 nm and 200 nm SiNPs may arise from interference fringes due to the presence of larger, spherical SiNPs in the ionomers. Results from these SANS experiments highlight how ion transport in these nanocomposites is not entirely governed by changes to the ionic network with the introduction of NPs, as conflicting trends between VO^{2+} permeability and ionic spacing were observed in many cases (e.g., Naf–AS–200 vs. Naf–AA–200). Results from this study have direct implications for the use of PFSA ionomer composites for VRFBs, for both fabrication methods that utilize less 'controllable' routes for NP formation, such as in situ sol-gel condensation, as well as for solution-cast ionomer nanocomposites, which are far less characterized in the literature.

CONFLICTS OF INTEREST

There are no conflicts to declare.

ACKNOWLEDGEMENTS

REFERENCES

(1)   Kusoglu, A.; Weber, A. Z. New Insights into Perfluorinated Sulfonic-Acid Ionomers. *Chem. Rev.* **2017**, *117*, 987–1104.

(2)   Paul, D. K.; Fraser, A.; Karan, K. Towards the Understanding of Proton Conduction Mechanism in PEMFC Catalyst Layer: Conductivity of Adsorbed Nafion Films. *Electrochem. Commun.* **2011**, *13* (8), 774–777. https://doi.org/10.1016/j.elecom.2011.04.022.

(3)   Tang, Z.; Keith, R.; Aaron, D. S.; Lawton, J. S.; Papandrew, A. P.; Zawodzinski Jr., T. A. Proton Exchange Membrane Performance Characterization in VRFB; 23; 2012; Vol. 41, pp 25–34. https://doi.org/10.1149/1.3697451.

(4)   Mauritz, K. A.; Moore, R. B. State of Understanding of Nafion. *Chem. Rev.* **2004**, *104* (10), 4535–4586. https://doi.org/10.1021/cr0207123.

(5)   Hickner, M. A. Water-Mediated Transport in Ion-Containing Polymers. *J. Polym. Sci. Part B Polym. Phys.* **2012**, *50* (1), 9–20. https://doi.org/10.1002/polb.22381.

(6)   Davis, E. M.; Kim, J.; Oleshko, V. P.; Page, K. A.; Soles, C. L. Uncovering the Structure of Nafion-SiO$_2$ Hybrid Ionomer Membranes for Prospective Large-Scale Energy Storage Devices. *Adv. Funct. Mater.* **2015**, *25* (26), 4064–4075. https://doi.org/10.1002/adfm.201501116.

(7)   Skyllas-Kazacos, M.; Kasherman, D.; Hong, D. R.; Kazacos, M. Characteristics and Performance of 1 KW UNSW Vanadium Redox Battery. *J. Power Sources* **1991**, *35* (4), 399–404. https://doi.org/10.1016/0378-7753(91)80058-6.

(8)   Allen, F. I.; Comolli, L. R.; Kusoglu, A.; Modestino, M. A.; Minor, A. M.; Weber, A. Z. Morphology of Hydrated As-Cast Nafion Revealed through Cryo Electron Tomography. *ACS Macro Lett.* **2015**, *4* (1), 1–5. https://doi.org/10.1021/mz500606h.

(9)   Equipment and Instruments or Materials Are Identified in the Paper in Order to Adequately Specify the Experimental Details. Such Identification Does Not Imply Recommendation by the National Institute of Standards and Technology (NIST), nor Does It Imply the Materials Are Necessarily the Best Available for the Purpose.

(10)   Trogadas, P.; Pinot, E.; Fuller, T. F. Composite, Solvent-Casted Nafion Membranes for Vanadium Redox Flow Batteries. *Electrochem. Solid-State Lett.* **2011**, *15* (1), A5–A8.

(11)   Xi, J.; Wu, Z.; Qiu, X.; Chen, L. Nafion/SiO2 Hybrid Membrane for Vanadium Redox Flow Battery. *J. Power Sources* **2007**, *166* (2), 531–536. https://doi.org/10.1016/j.jpowsour.2007.01.069.

(12)   Kushner, D. I.; Crothers, A. R.; Kusoglu, A.; Weber, A. Z. Transport Phenomena in Flow Battery Ion-Conducting Membranes. *Energy Storage ● Energy Transform.* **2020**, *21*, 132–139. https://doi.org/10.1016/j.coelec.2020.01.010.

(13)   Antonucci, P. L.; Aricò, A. S.; Cretì, P.; Ramunni, E.; Antonucci, V. Investigation of a Direct Methanol Fuel Cell Based on a Composite Nafion®-Silica Electrolyte for High Temperature Operation. *Solid State Ion.* **1999**, *125* (1), 431–437. https://doi.org/10.1016/S0167-2738(99)00206-4.

(14) Di Noto, V.; Bettiol, M.; Bassetto, F.; Boaretto, N.; Negro, E.; Lavina, S.; Bertasi, F. Hybrid Inorganic-Organic Nanocomposite Polymer Electrolytes Based on Nafion and Fluorinated TiO2 for PEMFCs. *Int. J. Hydrog. Energy* **2012**, *37* (7), 6169–6181. https://doi.org/10.1016/j.ijhydene.2011.07.131.

(15) Brinker, C. J.; Scherer, G. W. *Sol-Gel Science: The Physics and Chemistry of Sol-Gel Processing*; Academic Press, 2013.

(16) Deng, Q.; Moore, R. B.; Mauritz, K. A. Novel Nafion/ORMOSIL Hybrids via in Situ Sol-Gel Reactions. 1. Probe of ORMOSIL Phase Nanostructures by Infrared Spectroscopy. *Chem. Mater.* **1995**, *7* (12), 2259–2268.

(17) Mauritz, K. A.; Warren, R. M. Microstructural Evolution of a Silicon Oxide Phase in a Perfluorosulfonic Acid Ionomer by an in Situ Sol-Gel Reaction. 1. Infrared Spectroscopic Studies. *Macromolecules* **1989**, *22* (4), 1730–1734. https://doi.org/10.1021/ma00194a038.

(18) Ibrahim, I. A.; Zikry, A. A. F.; Sharaf, M. A. Preparation of Spherical Silica Nanoparticles: Stober Silica. *J Am Sci* **2010**, *6* (11), 985–989.

(19) Mauritz, K. A.; Stefanithis, I. D.; Davis, S. V.; Scheetz, R. W.; Pope, R. K.; Wilkes, G. L.; Huang, H.-H. Microstructural Evolution of a Silicon Oxide Phase in a Perfluorosulfonic Acid Ionomer by an in Situ Sol–Gel Reaction. *J. Appl. Polym. Sci.* **1995**, *55* (1), 181–190. https://doi.org/10.1002/app.1995.070550120.

(20) Mauritz, K. A.; Stefanithis, I. D. Microstructural Evolution of a Silicon Oxide Phase in a Perfluorosulfonic Acid Ionomer by an in Situ Sol-Gel Reaction. 2. Dielectric Relaxation Studies. *Macromolecules* **1990**, *23* (5), 1380–1388. https://doi.org/10.1021/ma00207a024.

(21) Jung, B.; Moon, H.-M.; Baroña, G. N. B. Effect of Methanol on Plasticization and Transport Properties of a Perfluorosulfonic Ion-Exchange Membrane. *J. Power Sources* **2011**, *196* (4), 1880–1885. https://doi.org/10.1016/j.jpowsour.2010.09.030.

(22) Young, S. K.; Trevino, S. F.; Tan, N. C. B. Small-Angle Neutron Scattering Investigation of Structural Changes in Nafion Membranes Induced by Swelling with Various Solvents. *J. Polym. Sci. Part B Polym. Phys.* **2002**, *40* (4), 387–400. https://doi.org/10.1002/polb.10092.

(23) Soniat, M.; Houle, F. A. Swelling and Diffusion during Methanol Sorption into Hydrated Nafion. *J. Phys. Chem. B* **2018**, *122* (34), 8255–8268. https://doi.org/10.1021/acs.jpcb.8b03169.

(24) Lovingood, D. D.; Owens, J. R.; Seeber, M.; Kornev, K. G.; Luzinov, I. Preparation of Silica Nanoparticles Through Microwave-Assisted Acid-Catalysis. *J. Vis. Exp. JoVE* **2013**, No. 82. https://doi.org/10.3791/51022.

(25) Stonehart, P.; Watanabe, M. Polymer Solid-Electrolyte Composition and Electrochemical Cell Using the Composition. 5523181, June 1996.

(26) Dimitrova, P.; Friedrich, K. A.; Stimming, U.; Vogt, B. Modified Nafion®-Based Membranes for Use in Direct Methanol Fuel Cells. *Solid State Ion.* **2002**, *150* (1), 115–122. https://doi.org/10.1016/S0167-2738(02)00267-9.

(27) Jansto, A.; Davis, E. M. Role of Surface Chemistry on Nanoparticle Dispersion and Vanadium Ion Crossover in Nafion Nanocomposite Membranes. *ACS Appl. Mater. Interfaces* **2018**, *10* (42), 36385–36397. https://doi.org/10.1021/acsami.8b11297.

(28) Domhoff, A.; Balwani, A.; Martin, T. B.; Davis, E. M. Leveraging Nanoparticle Dispersion State To Tune Vanadium Ion Selectivity of Nanophase-Segregated Ionomer Nanocomposites for Redox Flow Batteries. *ACS Appl. Energy Mater.* **2019**, *2* (12), 8535–8549. https://doi.org/10.1021/acsaem.9b01443.

(29) Kim, S.-O.; Kim, J. S. Preparation of Hybrid Proton Conductor by Sol-Gel Process from Nafion Solution. *Macromol. Res.* **2002**, *10* (3), 174–177. https://doi.org/10.1007/BF03218268.

(30) Adjemian, K. T.; Dominey, R.; Krishnan, L.; Ota, H.; Majsztrik, P.; Zhang, T.; Mann, J.; Kirby, B.; Gatto, L.; Velo-Simpson, M.; Leahy, J.; Srinivasan, S.; Benziger, J. B.; Bocarsly, A. B. Function and Characterization of Metal Oxide−Nafion Composite Membranes for Elevated-Temperature H_2/O_2 PEM Fuel Cells. *Chem. Mater.* **2006**, *18* (9), 2238–2248. https://doi.org/10.1021/cm051781b.

(31) Levy, D.; Zayat, M. *The Sol-Gel Handbook: Synthesis, Characterization, and Applications*; John Wiley & Sons, 2015.

(32) Jiang, B.; Wu, L.; Yu, L.; Qiu, X.; Xi, J. A Comparative Study of Nafion Series Membranes for Vanadium Redox Flow Batteries. *J. Membr. Sci.* **2016**, *510*, 18–26. https://doi.org/10.1016/j.memsci.2016.03.007.

(33) Teng, X.; Zhao, Y.; Xi, J.; Wu, Z.; Qiu, X.; Chen, L. Nafion/Organic Silica Modified TiO2 Composite Membrane for Vanadium Redox Flow Battery via in Situ Sol–Gel Reactions. *J. Membr. Sci.* **2009**, *341* (1–2), 149–154. https://doi.org/10.1016/j.memsci.2009.05.051.

(34) Teng, X.; Zhao, Y.; Xi, J.; Wu, Z.; Qiu, X.; Chen, L. Nafion/Organically Modified Silicate Hybrids Membrane for Vanadium Redox Flow Battery. *J. Power Sources* **2009**, *189* (2), 1240–1246. https://doi.org/10.1016/j.jpowsour.2008.12.040.

(35) Ladewig, B. P.; Knott, R. B.; Hill, A. J.; Riches, J. D.; White, J. W.; Martin, D. J.; Diniz da Costa, J. C.; Lu, G. Q. Physical and Electrochemical Characterization of Nanocomposite Membranes of Nafion and Functionalized Silicon Oxide. *Chem. Mater.* **2007**, *19* (9), 2372–2381. https://doi.org/10.1021/cm0628698.

(36) Rahman, I. A.; Vejayakumaran, P.; Sipaut, C. S.; Ismail, J.; Chee, C. K. Effect of the Drying Techniques on the Morphology of Silica Nanoparticles Synthesized via Sol–Gel Process. *Ceram. Int.* **2008**, *34* (8), 2059–2066. https://doi.org/10.1016/j.ceramint.2007.08.014.

(37) Qian, L.; Zhang, H. Controlled Freezing and Freeze Drying: A Versatile Route for Porous and Micro-/Nano-Structured Materials. *J. Chem. Technol. Biotechnol.* **2011**, *86* (2), 172–184. https://doi.org/10.1002/jctb.2495.

(38) Di Noto, V.; Gliubizzi, R.; Negro, E.; Pace, G. Effect of SiO2 on Relaxation Phenomena and Mechanism of Ion Conductivity of [Nafion/(SiO2)x] Composite Membranes. *J. Phys. Chem. B* **2006**, *110* (49), 24972–24986. https://doi.org/10.1021/jp0650331.

(39) Noto, V. D.; Piga, M.; Pace, G.; Negro, E.; Lavina, S. Dielectric Relaxations and Conductivity Mechanism of Nafion: Studies Based on Broadband Dielectric Spectroscopy. *ECS Trans.* **2008**, *16* (2), 1183. https://doi.org/10.1149/1.2981960.

(40) Balwani, A.; Davis, E. M. Anomalous, Multistage Liquid Water Diffusion and Ionomer Swelling Kinetics in Nafion and Nafion Nanocomposites. *ACS Appl. Polym. Mater.* **2020**, *2* (1), 40–54. https://doi.org/10.1021/acsapm.9b00866.

(41) Balwani, A.; Faraone, A.; Davis, E. M. Impact of Nanoparticles on the Segmental and Swelling Dynamics of Ionomer Nanocomposite Membranes. *Macromolecules* **2019**, *52* (5), 2120–2130. https://doi.org/10.1021/acs.macromol.8b02189.

(42) Rong, M. Z.; Zhang, M. Q.; Ruan, W. H. Surface Modification of Nanoscale Fillers for Improving Properties of Polymer Nanocomposites: A Review. *Mater. Sci. Technol.* **2006**, *22* (7), 787–796. https://doi.org/10.1179/174328406X101247.

(43)   Razmjou, A.; Mansouri, J.; Chen, V. The Effects of Mechanical and Chemical Modification of TiO2 Nanoparticles on the Surface Chemistry, Structure and Fouling Performance of PES Ultrafiltration Membranes. *J. Membr. Sci.* **2011**, *378* (1–2), 73–84. https://doi.org/10.1016/j.memsci.2010.10.019.

(44)   Tricoli, V. Proton and Methanol Transport in Poly (Perfluorosulfonate) Membranes Containing Cs+ and H+ Cations. *J. Electrochem. Soc.* **1998**, *145* (11), 3798–3801.

(45)   Liu, S.; Wang, L.; Ding, Y.; Liu, B.; Han, X.; Song, Y. Novel Sulfonated Poly (Ether Ether Keton)/Polyetherimide Acid-Base Blend Membranes for Vanadium Redox Flow Battery Applications. *Electrochimica Acta* **2014**, *130*, 90–96. https://doi.org/10.1016/j.electacta.2014.02.144.

(46)   Bukola, S.; Liang, Y.; Korzeniewski, C.; Harris, J.; Creager, S. Selective Proton/Deuteron Transport through Nafion|Graphene|Nafion Sandwich Structures at High Current Density. *J. Am. Chem. Soc.* **2018**, *140* (5), 1743–1752. https://doi.org/10.1021/jacs.7b10853.

(47)   Domhoff, A.; Davis, E. M. Influence of Casting Substrate on Bulk Morphology and Vanadium Ion Transport in Ionomer Nanocomposites. *J. Appl. Phys.* **2020**, *127* (17), 174701. https://doi.org/10.1063/1.5144204.

(48)   Kamcev, J.; Paul, D. R.; Freeman, B. D. Effect of Fixed Charge Group Concentration on Equilibrium Ion Sorption in Ion Exchange Membranes. *J. Mater. Chem. A* **2017**, *5* (9), 4638–4650. https://doi.org/10.1039/C6TA07954G.

(49)   Fujimoto, C.; Kim, S.; Stains, R.; Wei, X.; Li, L.; Yang, Z. G. Vanadium Redox Flow Battery Efficiency and Durability Studies of Sulfonated Diels Alder Poly(Phenylene)s. *Electrochem. Commun.* **2012**, *20*, 48–51. https://doi.org/10.1016/j.elecom.2012.03.037.

(50)   Zhang, Y.; Zhou, X.; Xue, R.; Yu, Q.; Jiang, F.; Zhong, Y. Proton Exchange Membranes with Ultra-Low Vanadium Ions Permeability Improved by Sulfated Zirconia for All Vanadium Redox Flow Battery. *Int. J. Hydrog. Energy* **2019**, *44* (12), 5997–6006. https://doi.org/10.1016/j.ijhydene.2019.01.043.

(51)   Yang, X.-B.; Zhao, L.; Goh, K.; Sui, X.-L.; Meng, L.-H.; Wang, Z.-B. A Highly Proton-/Vanadium-Selective Perfluorosulfonic Acid Membrane for Vanadium Redox Flow Batteries. *New J. Chem.* **2019**, *43* (28), 11374–11381. https://doi.org/10.1039/C9NJ01453E.

(52)   Yamazaki, K.; Tang, Y.; Kawakami, H. Proton Conductivity and Stability of Low-IEC Sulfonated Block Copolyimide Membrane. *J. Membr. Sci.* **2010**, *362* (1), 234–240. https://doi.org/10.1016/j.memsci.2010.06.053.

(53)   Lee, K. J.; Chu, Y. H. Preparation of the Graphene Oxide (GO)/Nafion Composite Membrane for the Vanadium Redox Flow Battery (VRB) System. *Vacuum* **2014**, *107*, 269–276. https://doi.org/10.1016/j.vacuum.2014.02.023.

(54)   Galizia, M.; Manning, G. S.; Paul, D. R.; Freeman, B. D. Ion Partitioning between Brines and Ion Exchange Polymers. *Polymer* **2019**, *165*, 91–100. https://doi.org/10.1016/j.polymer.2019.01.026.

(55)   Galizia, M.; Benedetti, F. M.; Paul, D. R.; Freeman, B. D. Monovalent and Divalent Ion Sorption in a Cation Exchange Membrane Based on Cross-Linked Poly (p-Styrene Sulfonate-Co-Divinylbenzene). *J. Membr. Sci.* **2017**, *535*, 132–142. https://doi.org/10.1016/j.memsci.2017.04.007.

(56)   Kamcev, J.; Galizia, M.; Benedetti, F. M.; Jang, E.-S.; Paul, D. R.; Freeman, B. D.; Manning, G. S. Partitioning of Mobile Ions between Ion Exchange Polymers and Aqueous

Salt Solutions: Importance of Counter-Ion Condensation. *Phys. Chem. Chem. Phys.* **2016**, *18* (8), 6021–6031. https://doi.org/10.1039/C5CP06747B.

(57) Domhoff, A.; Martin, T. B.; Silva, M. S.; Saberi, M.; Creager, S.; Davis, E. M. Enhanced Proton Selectivity in Ionomer Nanocomposites Containing Hydrophobically Functionalized Silica Nanoparticles. *Macromolecules* **2021**, *54* (1), 440–449. https://doi.org/10.1021/acs.macromol.0c01696.